International Journal of Solids and Structures 234-235 (2022) 111252

Contents lists available at ScienceDirect

International Journal of Solids and Structures

journal homepage: www.elsevier.com/locate/ijsolstr

Cascading crack bifurcations in soda-lime glass: Quantification of fracture mechanics-based precursors using Digital Gradient Sensing

S. Dondeti, H.V. Tippur *

Department of Mechanical Engineering, Auburn University, AL 36849, United States

ARTICLE INFO

Keywords:
Dynamic fracture
Crack branching precursors
Cascading bifurcations
Soda-lime glass
Digital Gradient Sensing

ABSTRACT

Dynamic crack growth in high-stiffness and ultralow-toughness amorphous materials such as soda-lime glass (SLG) often involves seemingly unprovoked crack branching events which are yet to be fully explained. The absence of optical tools for performing mechanical field measurements at sufficiently high spatial and temporal resolutions to decipher highly localized deformations at the tip of a crack growing in excess of mile-a-second speed has perpetuated this knowledge gap. The full-field method of Digital Gradient Sensing (DGS) used in conjunction with ultrahigh-speed photography has overcome some of these limitations allowing direct quantification of fracture parameters associated with different phases of crack growth in SLG (Sundaram and Tippur, 2018; Dondeti and Tippur, 2020). In this work, time-resolved stress gradients are measured in SLG plates of two different geometries, first one producing a single crack bifurcation event and the second two-tier cascading crack bifurcations, during dynamic wedge-loading experiments. The measurements are then used along with the asymptotic crack-tip fields to extract fracture parameters and identify crack branching precursors based on crack velocity, stress intensity factors, and higher order coefficients. The fracture surface roughness and other features are also separately quantified via high-resolution post-mortem examination to corroborate them with the optically measured quantities.

1. Introduction

Despite their widespread use in structural and engineering applications, more needs to be understood about crack branching phenomenon in brittle materials such as soda-lime glass (SLG). This is primarily due to the fact that investigation of dynamic crack branching in SLG is extremely challenging owing to severe spatial and temporal resolution requirements. That is, (a) cracks often propagate at speeds exceeding 1500 m/s in SLG, and (b) the crack-tip opening displacements and deformations near a growing crack-tip are extremely small, in the nano- to sub-micron scale. Due to these challenges, many early investigators carried out their studies on amorphous quasi-brittle polymers instead despite the intrinsic viscous effects and microscopic inhomogeneities (Rose, 1976). Dally (1979) reported dynamic fracture of Homalite-100 using photoelasticity and concluded that a crack branched when mode-I stress intensity factor reached its crack branching toughness. Ramulu et al. (1984) also investigated crack branching in Homalite-100 photoelastically, and proposed a necessary condition for branching based on a critical dynamic stress intensity factor and a sufficient condition of minimum characteristic distance for crack curving. Furthermore, they verified their crack branching criteria using centrally cracked specimens subjected to biaxial loading (Hawong et al., 1987). Ravi-Chandar and Knauss (1984) investigated dynamic fracture of Homalite-100 using the method of optical caustics and proposed that a crack propagating with a sufficiently high stress intensity factor excites voids and other defects ahead of the moving crack-tip to generate microcracks. They attributed the interaction of these microcracks with the main crack to cause macroscale crack branching. Theocaris et al. (1989) proposed another crack branching idea based on macroscopic fracture energy criteria and applied it to the branched tips to determine the expected angle of crack propagation. It was based on the assumption that at early stages of crack propagation, a tuft of microcracks would form ahead of the main propagating crack, out of which two symmetric microcracks prevail over the others causing macroscale crack branching. Recently, Sundaram and Tippur (2016) investigated dynamic crack-interface interactions in PMMA bilayers using the optical method of Digital Gradient Sensing (DGS). They observed two different crack growth behaviors past a weak interface perpendicular to the incoming

* Corresponding author.
E-mail address: tippuhv@auburn.edu (H.V. Tippur).

https://doi.org/10.1016/j.ijsolstr.2021.111252
Received 10 January 2021; Received in revised form 25 July 2021; Accepted 6 September 2021
Available online 11 September 2021

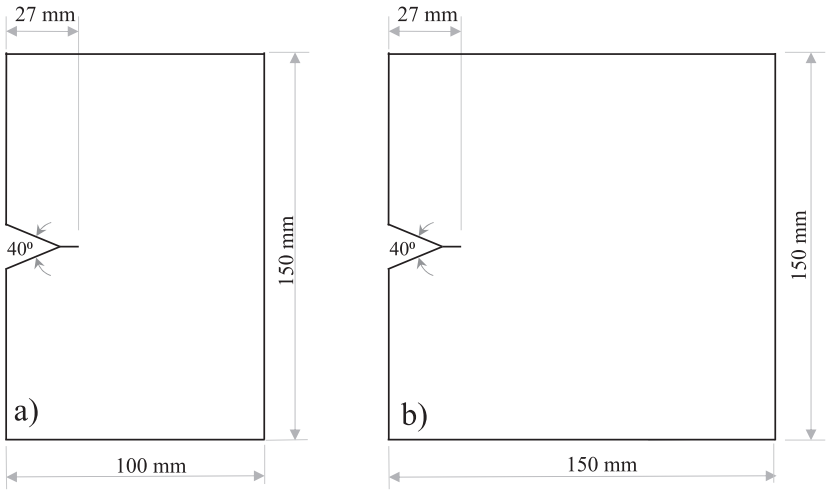

Fig. 1. Two soda-lime glass specimen geometries (a) and (b) with extended V-notch. (Plate thickness = 5.7 mm; extended notch length = 8 mm).

mode-I crack namely, penetration of the interface without branching or interfacial crack growth followed by macroscale branching. The measured crack-tip parameters showed that if the interface experienced stress waves in excess of its tensile strength, a debond nucleated at the interface *prior* to the arrival of the mode-I mother crack resulting in mixed-mode crack growth and subsequent branching; otherwise no macroscale branching occurred.

Some earlier studies have reported on crack branching in highly brittle materials such as rocks and glass. For example, Bieniawski (1968) investigated dynamic crack branching in rocks and reported that a crack branched upon reaching a terminal velocity. Using a multiple-spark high-speed camera Schardin (1959) studied fracture of glass and observed that the crack propagated with a constant velocity of ~1500 m/s. And, in the presence of an imposed far-field tensile stress, the crack propagated for a shorter distance before branching and the number of branches increased with the applied stress. In another study, Döll (1975) investigated crack propagation in different glasses - plate glass, FK-52 and Duran 50 – and noted that crack branching depended on (a) the crack attaining a maximum velocity and, (b) the strain energy release rate exceeding a critical value. Sundaram and Tippur, 2018a, 2018b were the first to quantitatively study crack-tip fields in soda-lime glass (SLG) using a full-field optical technique. They coupled DGS technique with ultrahigh-speed photography to investigate dynamic crack initiation and growth. They were able to quantify not only crack velocities but fracture parameters namely, stress intensity factor and energy release rate histories, from the start to the finish that included crack initiation, mode-I crack growth and mixed-mode crack branching. More recently, Dondeti and Tippur (2020) revisited the problem of dynamic fracture in SLG using photoelasticity, 2D-DIC and DGS methods and concluded that DGS was able to visualize and quantify dynamic fracture parameters with good precision without the shortcoming of the other two methods.

Several analytical studies on dynamic crack branching of brittle materials have been carried out by various researchers. Yoffe and LXXV (1951) investigated a straight crack moving through an elastic medium and described the stress fields around the propagating crack. She observed that the crack tended to curve when propagating at a critical velocity of $\sim 0.6C_s$ (C_s = shear wave speed) with the maximum hoop stress occurring at 60° relative to the self-similar crack growth direction. Eshelby et al. (1999) reviewed some of the energy relations and evaluated the energy required for dynamic crack branching based on elastic energy–momentum tensors.

In addition to the above experimental and analytical contributions, a considerable amount of data has been generated over the years from numerical simulations. Xu and Needleman (1994) studied dynamic crack branching in PMMA using cohesive elements. They found that the crack velocities reached ~45% of the Rayleigh wave speed at branching. Furthermore, their study revealed crack speed oscillations that eventually led to crack branching at an angle of 29° from the initial crack plane. When the crack growth was restricted to the crack plane, the crack accelerated initially and then propagated at a constant velocity. Zhou and Molinari (2004) also studied dynamic brittle fracture by introducing cohesive elements into their finite element model to address mesh dependency. Recently, Zeng et al. (2019) simulated dynamic crack propagation in brittle and quasi-brittle materials using embedded finite element method (EFEM) and extended finite element method (XFEM). They concluded that the crack growth history from XFEM agreed better with the experimental data than EFEM. The phase-field method was employed by Karma and Lobkovsky (2004) to simulate dynamic brittle fracture of mode III cracks. Their simulations show occurrence of branching instability at a fraction of the wave speed. Ha and Bobaru (2010) employed peridynamics to investigate dynamic crack branching in soda-lime glass. They noted that branching patterns correlated well with that of experimental results in addition to crack propagation velocities. Furthermore, they noticed that branching occurred in a region where crack propagation velocities reached higher fraction of the maximum value along with roughening of the fractured surface before crack branching and a detectable reduction in crack velocities after the crack branching event. Bobaru and Zhang (2015) also noted that, as the stress intensity factor around the crack-tip increased, the stress waves piled-up directly ahead of the crack-tip. This caused the maximum strain energy to shift away from the line-of-symmetry causing the crack to deviate from the crack line. Most recently, Mehrmashhadi et al. (2020) analyzed dynamic fracture in brittle materials using three different computational models, and compared their results to full-field optical investigation of dynamic crack initiation, propagation and branching in soda-lime glass reported by Sundaram and Tippur, 2018a. They concluded that the peridynamic model matched many details from the observed fracture patterns.

A full-field optical investigation of dynamic crack branching in SLG was undertaken in this work using geometries capable of producing single and cascading bifurcations when subjected to stress wave loading. The intent of the work is to bridge gaps in our understanding of the crack branching event via direct quantification of fracture mechanics-based precursors associated with the primary and secondary bifurcations in a single experiment. The details of the experimental setup and procedure adopted for performing the optical measurements are presented next. Evaluation of dynamic fracture parameters in single and cascading branch formations from optical measurements is described after that. Some plausible crack branching precursors are quantified subsequently. The post-mortem fractographic observations and quantifications are

Table 1
Nominal soda-lime glass properties.

Property	Value
Density, ρ	2500 kg/m^3
Longitudinal wave speed, C_L	5700 m/s
Shear wave speed, C_S	3400 m/s
Rayleigh wave speed, C_R	3100 m/s
Elastic modulus, E	70 GPa
Poisson's ratio, υ	0.22
Tensile strength, σ_t	40–180 MPa
Compressive strength, σ_c	330 MPa
Elasto-optic constant, C_σ	-0.027×10^{-10} m^2/N

also included at the end and corroborated with the measured fracture parameters leading up to crack branching.

2. Experimental

2.1. Specimen geometries

Transparent SLG plates used to study dynamic mode-I crack branching were commercially procured. Specimens were cut from a single large 5.7 mm thick plate into samples of two different dimensions: (a) 150 mm length, and 100 mm width, and (b) 150 mm length, and 150 mm width. A symmetric 40° V-notch was introduced at the mid-span of each specimen type along the 150 mm edge, as shown in Fig. 1. The apex of the V-notch was extended by 8 mm using a 0.3 mm thick diamond impregnated circular saw. Some mechanical and physical properties of SLG relevant to this work are listed in Table 1.

2.2. Digital Gradient Sensing (DGS) method

Transmission-mode Digital Gradient Sensing (DGS) technique (Periasamy and Tippur, 2013) was used in this work to visualize and quantify crack-tip fields associated with crack initiation, growth, and branching phenomena. This technique utilizes 2D DIC to quantify perceived speckle shifts that are proportional to orthogonal in-plane stress gradients when observed through planar specimens. A random speckle decoration on a planar surface (*not* on the transparent specimen) called the 'target' is photographed through the region-of-interest (ROI) in specimen, see Fig. 2. The gray scales on the target are illuminated using polychromatic lamps. The speckle pattern on the target is photographed first through the unstressed (reference) specimen. That is, the gray scale information at a point P on the target plane (x_0-y_0 plane) through a point O on the specimen plane (x-y plane) is captured by the camera. Upon loading, the non-uniform state-of-stress alters the refractive index of the specimen locally, say, in the crack-tip vicinity. In addition, the specimen thickness changes non-uniformly in the ROI due to the Poisson effect. A combination of these two phenomena, commonly referred to as the elasto-optic effect, make the light rays to deviate from their original path as they propagate through the stressed specimen. The speckle pattern is once again photographed through the specimen in the stressed state to record the gray scale at a neighboring point Q on the target through the same point O on the specimen. By correlating the speckle images in the reference and stressed states, local shifts in speckle clusters, δ_x and δ_y, are quantified using speckle/image correlation algorithms. Knowing the distance between the specimen and the target planes from the experimental setup, the angular deflections of the light rays ϕ_x and ϕ_y in two orthogonal planes (x-z and y-z planes, the z-axis coinciding with the optical axis of the setup and x-y being the specimen plane coordinates) are evaluated. These angular deflections are shown to be proportional to the gradients of the in-plane normal stresses as,

$$\phi_{x,y} = \pm C_\sigma B \frac{\partial(\sigma_x + \sigma_y)}{\partial x; y}, \tag{1}$$

where C_σ is the elasto-optic constant of the material, B is its initial thickness, $(\sigma_x + \sigma_y)$ is the first stress invariant under plane stress condition, and σ_x and σ_y denote the thickness-wise averages of Cauchy's normal stress components.

It is important to note that while recording speckles, the camera is focused on the target through the transparent specimen. However, to perform analysis of the mechanical fields, they are needed in terms of the specimen plane coordinates. This is achieved by mapping P(x_o, y_o) on the target plane to point O(x, y) on the specimen using the so-called pin-hole camera approximation. The mapping function between the specimen and the target planes is, $(x; y) \times (L + \Delta) = (x_o; y_o) \times L$ where L and Δ represent distances between the camera and the specimen and specimen and the target planes, respectively.

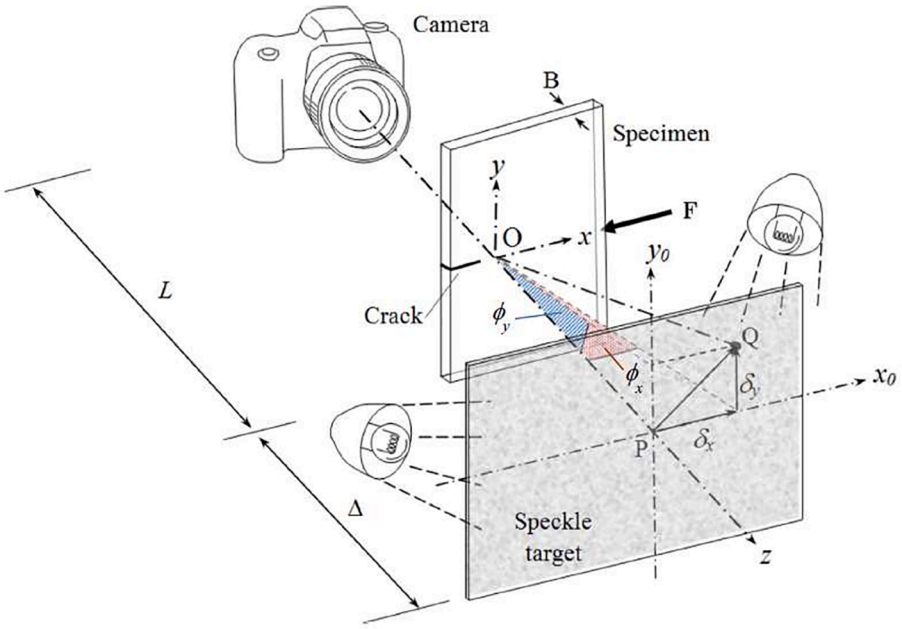

Fig. 2. The schematic representation of Digital Gradient sensing (DGS) technique to determine planar stress gradients.

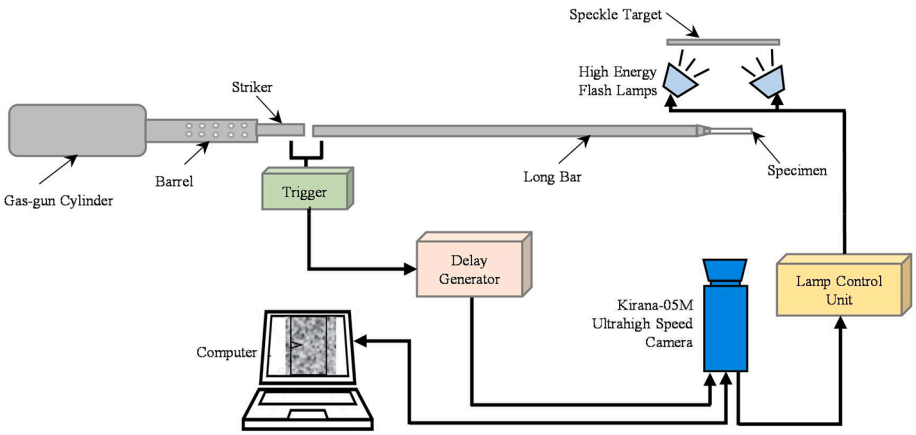

Fig. 3. The schematic of experimental setup for transmission DGS measurements.

2.3. Experimental setup

A schematic representation of the experimental setup is shown in Fig. 3. Experiments were performed using a modified Hopkinson pressure bar or a long-bar impactor (1830 mm long and 25.4 mm diameter C-300 maraging steel rod) in conjunction with DGS and ultrahigh-speed photography. The long-bar had a wedge shaped blunt tip (20° taper) for insertion into the V-notch cut-into the specimen. The specimen was placed on ~4 mm thick putty strip on a translation stage to align the specimen relative to the long-bar. Another strip of putty was pressed onto the top edge of the specimen to create symmetry in terms of acoustic impedance on the opposing edges relative to the loading axis. Other than the V-notch flanks, all other specimen edges were free. The loading phase, crack initiation[1], mode-I crack growth leading to mixed-mode branching were all recorded using the ultrahigh-speed camera for a loading pulse duration of ~120 μs in the 100 mm × 150 mm specimen geometry. In the 150 mm × 150 mm specimen geometry, however, the temporal window of interest covered mode-I crack growth, and first and subsequent crack branching events. When the striker (A 305 mm long, 25.4 mm diameter steel cylinder) impacted the long-bar with a velocity of 6 m/s, a trigger pulse was generated to start the camera recording and capture the speckle images off the target plane through the specimen. The ultrahigh-speed camera simultaneously triggered a pair of xenon high-energy flash lamps. A delay generator was also used in the trigger circuit since the stress waves need to propagate the length of the long-bar before loading the specimen. In these experiments, a delay of 320 μs was used. A Kirana-05 M ultrahigh-speed digital camera with 924 × 768 pixels sensor operating at 1 million frames per second, and 10-bit gray scale resolution recorded 180 full resolution images. The camera was positioned perpendicular to the specimen at a distance of 3.86 m in front of the specimen, whereas the speckle target was at a distance of 1.0 m behind the specimen. A Nikkor 400 mm focal length, $F^{\#}$2.8 lens along with a focal length doubler and adjustable bellows were used to record speckles on the target plate. After focusing the camera on the speckles, the aperture opening was reduced to $F^{\#}$16 to further increase the depth-of-focus while maintaining satisfactory exposure. A 110 × 92 mm^2 region on the target corresponding to approx. 88 × 65 mm^2 on the specimen, was photographed. The resulting magnification factor (or the scale factor) of these images was 123 μm/pixel. Besides monitoring the contact stress evolution on the crack flanks (Dondeti and Tippur, 2020), the ROI covered crack initiation, mode-I crack propagation of the mother crack leading to two mixed-mode daughter crack/branch formation in the first geometry (100 mm × 150 mm specimen). In the second geometry (150 mm × 150 mm specimen), the size of the ROI was maintained the same but was advanced into the middle of the specimen to be able to capture some of the mode-I mother crack growth before branching, first mixed-mode daughter crack branch formation and then the evolution of *a pair* of cascading mixed-mode granddaughter cracks and their growth.

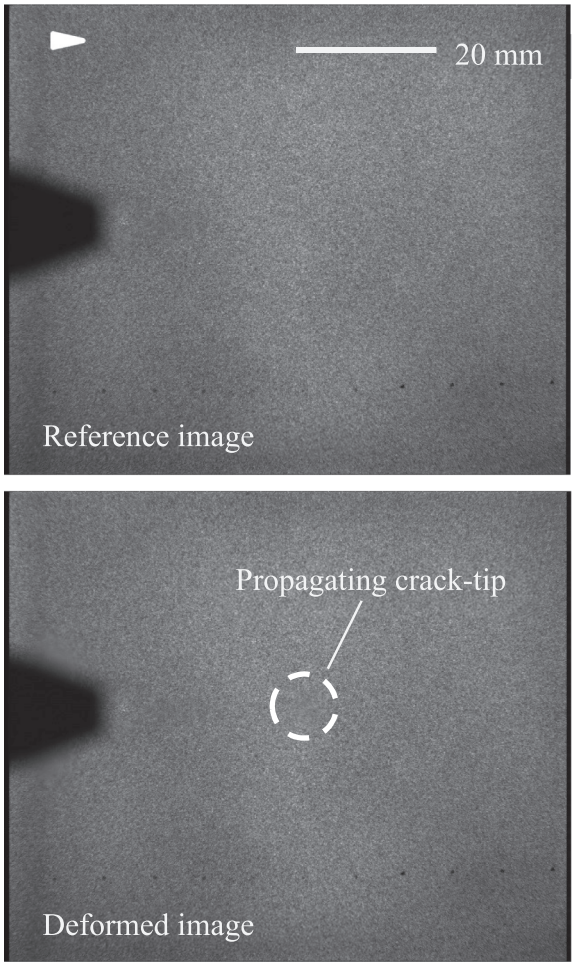

Fig. 4. Speckle images from DGS in the undeformed (top) and deformed (bottom) states for propagating crack-tip recorded by the ultrahigh-speed camera through the soda-lime glass specimen. (Arrowhead shows the overall crack growth direction).

[1] Based on the load history on notch flanks reported in [2] for this experiment, it takes ~25μsec after the start of the compressive notch flank loading to initiate the crack in the 100 mm wide sample. This corresponds to the reflected, tensile (longitudinal) waves to reach the notch tip.

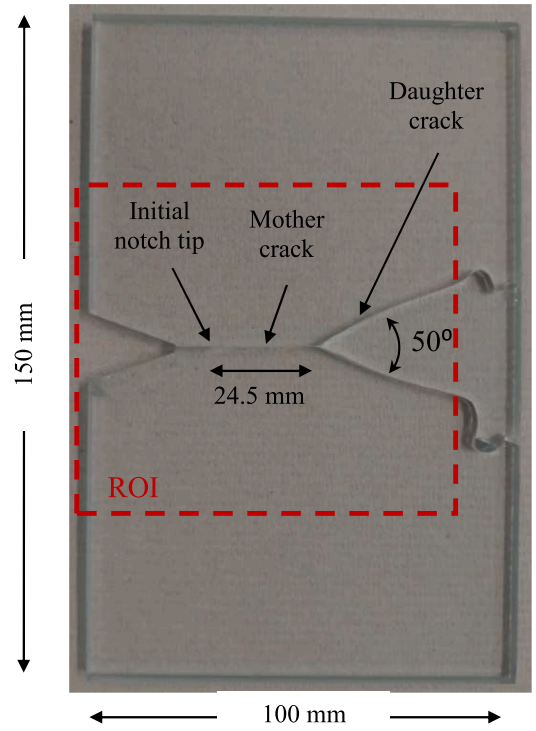

Fig. 5. Photograph of reassembled fractured soda-lime glass specimen with a single crack branching event.

3. Stress gradient and crack speed histories

3.1. 100 mm × 150 mm specimen

Two representative speckle images, one in the reference and the other in the stressed state of the specimen, are shown in Fig. 4. These speckle images are provided for completeness only and are not visually informative. That is, neither the stationary nor the growing crack-tip is discernible except for a blob of distorted speckles in the specklegram corresponding to the stress state relative to the reference, when observed carefully. This is because the camera is focused on the target instead of the specimen. Therefore, the angular deflections of light rays and hence stress gradient fields become apparent only after correlating the speckle images. A photograph of the fractured specimen from this experiment is shown in Fig. 5. After initiating from the notch-tip, the crack propagated as a mode-I mother crack and subsequently bifurcated into two dominant mixed-mode daughter cracks at a distance of approx. 25 mm from the initial tip. The branched cracks maintained global symmetry relative to the mother crack with an angle of ~50° between them, see Fig. 5. Finally, when the two daughter cracks approached the specimen edge, the crack paths became unstable resulting in waviness due to the loss of in-plane constraint.

The angular deflections of light rays, $\phi_x$and ϕ_y, in two orthogonal directions (with respect to mode-I propagating mother crack) along with the resultant values of angular deflections $\phi_r\,(=\sqrt{\phi_x^2+\phi_y^2})$ at select time instants, are shown in Fig. 6 as contour maps. These contour maps were obtained by segmenting the speckle images in the reference and deformed states, recorded at different time instants, into 30 × 30 pixel sub-images. The scale factor of these images was 123 μm/pixel. The location of a sub-image in the deformed state was determined relative to its position in the reference state by performing 2D gray scale correlation using commercial image analysis software ARAMIS® (GOM mbH, Braunschweig, Germany). An overlap of 5 pixels was used during analysis. Once the location of a sub-image in the deformed state was identified, the local speckle shifts were quantified at the center of each sub-image. This resulted in u and v displacement data arrays corresponding to horizontal and vertical directions, respectively, each of 147 × 178 size in the ROI. These were subsequently converted into ϕ_x and ϕ_y by dividing u and v by the gap between the specimen and target planes in the optical setup. Using 2% of the scale factor (=123 μm/pixel) as the limit of 2D DIC method's capability for detecting speckle shifts accurately, the lowest angular deflections of light rays measurable is ~2.5×10^{-6} rad. The first column in Fig. 6 corresponds to mode-I crack propagation of the mother crack (before branching) at time $\tau = -13$ μs whereas the second column represents mixed-mode crack propagation of the two daughter cracks (after branching) at time $\tau = 7$ μs. Here, the timestamps are with respect to the time instant when crack branching occurred or $\tau = 0$. (Note that the data in the whole field was available as rectangular arrays at each time instant and are plotted as contours via post-processing.) A video animation encompassing the evolution of stress gradients along the two V-notch flanks[2], and near the crack-tip at initiation, during growth and branching events are available in the supplementary materials section of the paper. The ϕ_x contours are symmetric relative to the dominant mode-I crack path whereas ϕ_y contours are antisymmetric for the mother crack. Once the crack branched, both sets of contours became asymmetric relative to the mixed-mode daughter cracks. Locating the crack-tip from these DGS contours is rather obvious due to the singular nature of the stress gradient fields (Sundaram and Tippur, 2018c). That is, the contours representing each of the measured fields have closed-lobe structures converging to the crack-tip, marked in Fig. 6 (and the supplementary material) by a solid white dot/circle, making it relatively easy to locate it at each time instant from any of the three fields. That is, as can be seen from Fig. 6, once the deformation contours are plotted, the instantaneous crack-tip position becomes self-evident. (In this work, ϕ_r contours were used to locate the crack-tip and track the crack path.) To assess the error associated with instantaneous crack-tip position, stress gradient contours were plotted at each time step in three different increments (4, 8, 12 micro-radians) and the crack-tip was identified. The scatter in the crack tip location in these three measurements was then used to estimate the likely error in instantaneous velocity.

The apparent crack length and velocity histories are shown in Fig. 7 (a) and (b), respectively, including the error bars. The crack length increased monotonically until the end of the observation window. A subtle kink in the crack length history between $\tau = -4$ to -1 μs can be seen before the crack branched. Subsequently, the crack length increased steadily. The crack-tip locations of the two mixed-mode daughter cracks were such that the instantaneous crack lengths overlapped with each other as the two daughter cracks grew symmetrically relative to the mode-I mother crack. The crack length histories were smoothed using Bezier curves (Prautzsch et al., 2013) and then the apparent crack velocity (V) histories were extracted using the backward difference method, see Fig. 7(b). The crack accelerated to ~1530 m/s over ~4 μs duration following initiation. Subsequently, the crack maintained an average velocity of 1400–1550 m/s in the pre-branching phase, consistent with those reported in Refs. (Dondeti and Tippur, 2020; Miao and Tippur, 2020; Schardin, 1959; Sundaram and Tippur, 2018a). As the crack entered the branching phase between $\tau = -4$ to -1 μs, the apparent crack velocity gradually reduced, to values between 1250 and 1050 m/s. This dip in the crack speed prior to the crack branching event stands out as a potential precursor of impending crack

[2] The stress gradient contours adjacent to the two V-notch flanks suggest that the contact between the long-bar and the specimen has resulted in a (compressive) line-load acting at about 5 mm from the left edge of the specimen. Details on estimated load history from these contours is reported in Ref. [2].

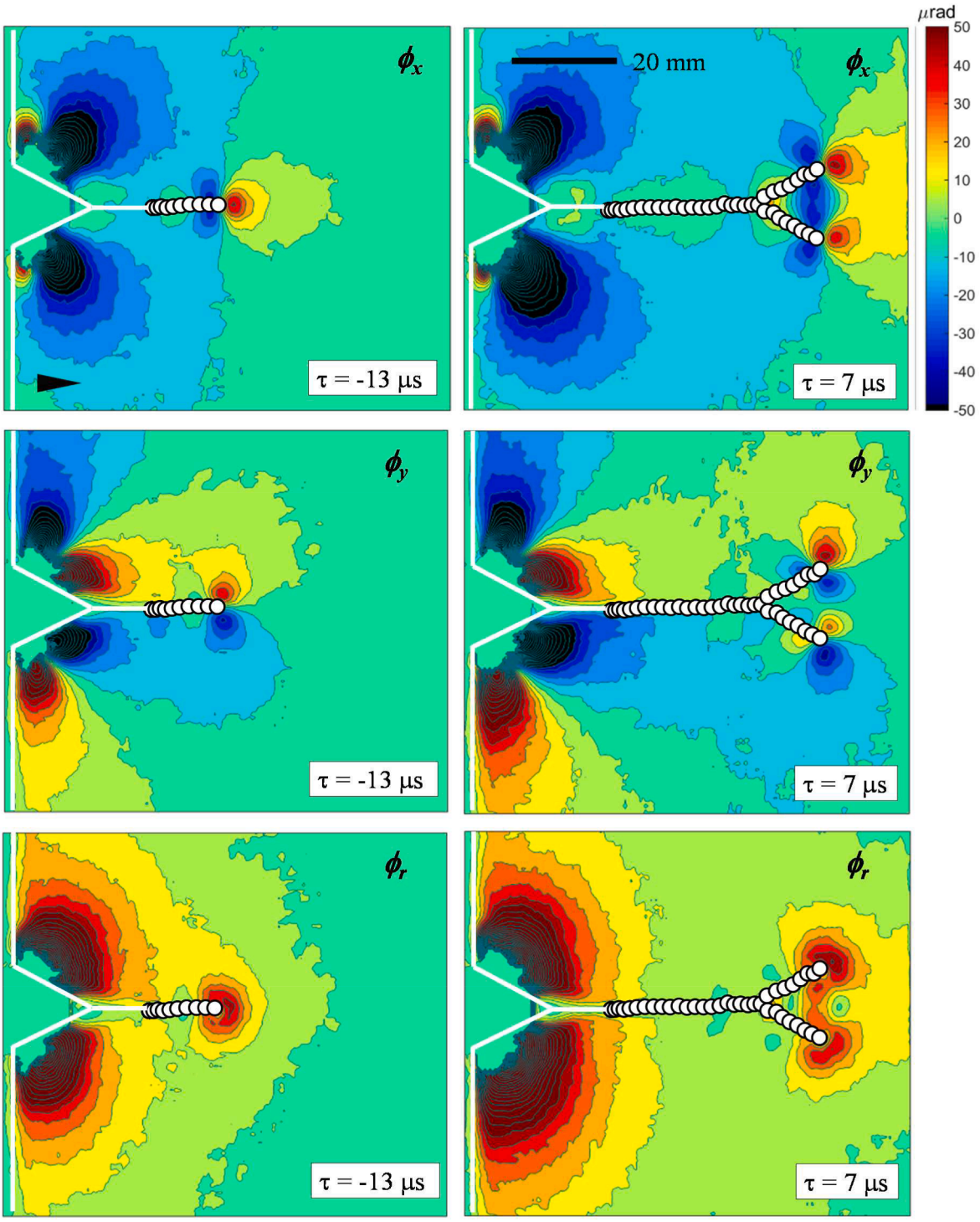

Fig. 6. Contours of angular deflections of light rays (contour increment = 8×10^{-6} rad) in 100 mm × 150 mm soda-lime glass plate. The arrowhead (in the top left image) shows crack growth direction. White markers indicate crack-tip locations in the previous frames. ($\tau = 0$ corresponds to crack branching of the mother crack.)

bifurcation. Soon after this dip, the crack branched into two angled mixed-mode daughter cracks, both accelerated to ~1700 m/s almost instantaneously[3]. The two daughter cracks subsequently decelerated back to ~1500 m/s until the end of the observation window and no further crack velocity reduction similar to the mother crack was seen. These trends have been highlighted in the plots using thick broken lines or shaded circles superposed on instantaneous values[4].

3.2. 150 mm × 150 mm specimen

A photograph of the fractured specimen from the experiment is

[3] The velocity data for ~3μs soon after branching is more ambiguous relative to the pre-branching counterparts. The maximum error in crack velocity was 80–90 m/s with most data showing a scatter in the 50 m/s range.

[4] Note that some liberty has been exercised while highlighting these trends for interpretation purposes.

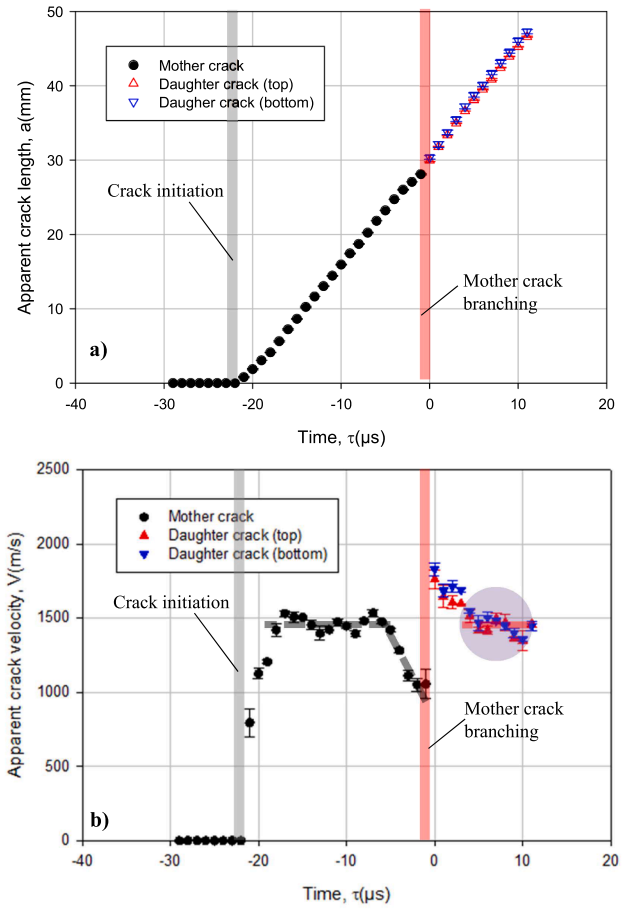

Fig. 7. Apparent crack length (top) and crack velocity (bottom) histories for 100 mm × 150 mm soda-lime glass plate. ($\tau = 0$ corresponds to mother crack branching event; the heavy broken lines suggest data trends; data uncertainty for ~3 μs after branching is higher than the rest.)

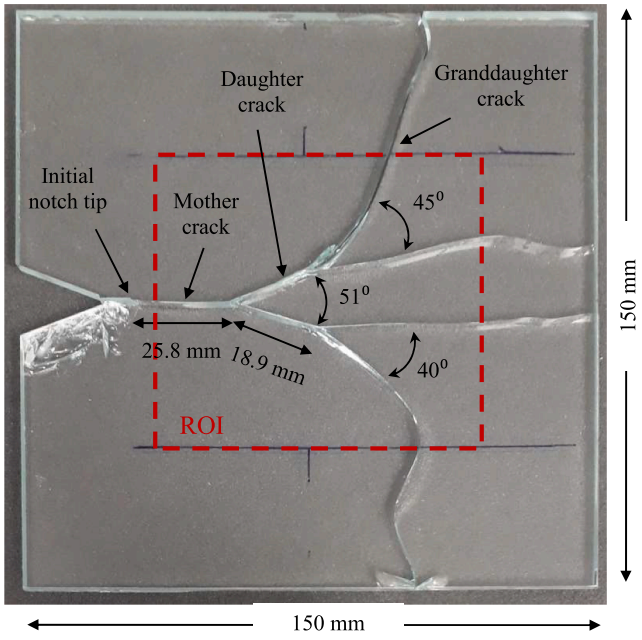

Fig. 8. Photograph of the reconstructed fractured soda-lime glass specimen with cascading crack bifurcations.

shown in Fig. 8. Evidently, after initiating at the original notch-tip located outside the ROI, the mother crack first propagated as a nominally mode-I crack and subsequently branched into two mixed-mode daughter cracks at a distance of approx. 26 mm from the initial tip. The daughter cracks maintained global symmetry relative to the mother crack, with an angle of ~51° between them[5], as evident in Fig. 8. These features are rather similar to the 100 mm × 150 mm specimen even though the specimen geometry is different. Both the daughter cracks, after propagating over a distance of approx. 20 mm, branched/bifurcated again and produced two dominant granddaughter cracks each, resulting in four simultaneously propagating crack-tips in the ROI. These granddaughter cracks were somewhat less symmetric relative to the daughter cracks when compared to the daughter cracks relative to the mother crack. Yet, given the unavoidable loading/setup asymmetries and local material anomalies, the overall symmetry achieved in terms of the crack branch formations is rather noteworthy.

In order to ascertain the repeatability of this test, additional tests on 150 mm × 150 mm geometry were carried out and for brevity, results from one other experiment is included in the section on supplementary materials (see, Fig. S1). The reader is directed to examine those results side-by-side the rest of the analysis presented next.

The angular deflections of light rays, ϕ_x and ϕ_y, in the two orthogonal directions (with respect to mode-I propagating mother crack) at three select time instants, are shown in Fig. 9 as contour maps. (The image analysis parameters are same as the ones discussed previously.) The first row in the figure corresponds to mode-I crack propagation of the mother crack (before branching) at a time instant $\tau = -5$ μs whereas the second row corresponds to mixed-mode propagation of the two daughter cracks (subsequent to the first branching event) at $\tau = 9$ μs. The last row corresponds to mixed-mode propagation of all four granddaughter cracks (after the second branching event) at $\tau = 25$ μs. (*Note that $\tau = 0$ corresponds to the first crack branching event.*) The solid white dots are again superposed on the stress gradient contours to represent the location of crack-tips at the current and prior time instants to help visualize the histories during the fracture event. A video animation of the entire fracture evolution including mode-I crack growth and the two crack branching events resulting in two daughter cracks and four granddaughter cracks is available in the supplementary materials section. (The angular deflection contours for the repeatability experiment can be found in Fig. S2.) Again, the ϕ_x contours are symmetric relative to the mother crack path whereas ϕ_y contours are antisymmetric. The two daughter as well as the four granddaughter crack-tip fields are all asymmetric relative to the mother crack. As in the 100 mm × 150 mm specimen, contours of ϕ_r (not shown for brevity) were plotted at each time instant and used to locate the crack-tip and track the crack path by a series of successive white dots.

The apparent crack velocity histories are shown in Fig. 10. As the propagating mother crack entered the observation window (solid black circles), the crack was already slowing down from around 1500 m/s to ~1000 m/s (over ~ 6 μs), prior to branching. This behavior is consistent with that seen in the 100 mm × 150 mm geometry (see, Fig. 7(b)). Once the crack branched first (at $\tau = 0$), the velocities of the two daughter cracks (solid blue and red triangles, upright triangles for the upper branch, inverted triangles for the lower branch) jump to ~1900 m/s but rapidly decelerate to ~1500 m/s and continue propagating at this speed for the next 4 to 5 μs. Subsequently, a second slowing trend, again from ~1500 m/s to ~1000 m/s over the next 6–7 μs, for both the daughter cracks is evident. (The lower branch traveled at a higher velocity relative to the upper branch, possibly due to experimental anomalies.) The reduction in the crack speed prior to the second pair of crack branching events is consistent with that for the mother crack and can be identified

[5] A similar crack branching pattern with somewhat lower degree of symmetry and angular separations was seen in other experiments, details for one of those is included in the supplementary materials section.

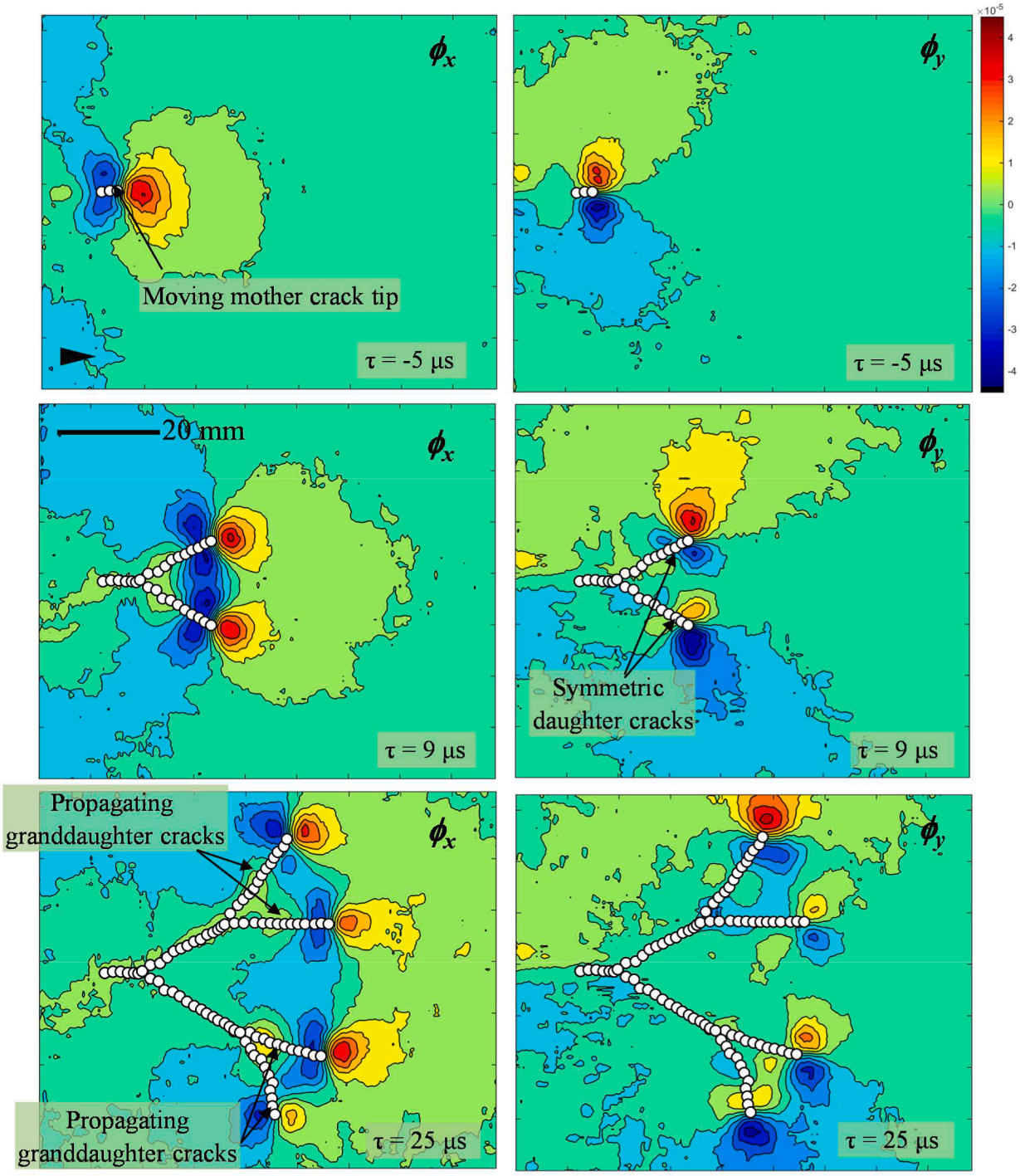

Fig. 9. Angular deflection contours (contour interval = 7×10^{-6} rad) in 150 mm × 150 mm soda-lime glass plate. The arrowhead (in the top left image) shows crack growth direction. White markers indicate crack-tip locations in the previous frames. ($\tau = 0$ corresponds to crack branching event.)

again as a precursor of branching event. The second branching event occurred between 13 and 15 μs; the upper branch bifurcated first followed by the lower branch a couple of microseconds later. Once branching occurred, each granddaughter crack accelerated to ~2000 m/s, again consistent with the first branching event at $\tau = 0$. A gradual deceleration of granddaughter cracks to a steady 1500 m/s is evident for the rest of the observation window without further slowing down. Accordingly, based on the characteristics noted during the previous three branching events, no further branching should occur and this pattern indeed holds true. That is, from the photograph of the fractured specimen, it is clear that no further branching occurred outside the observation window. Again, note that approximate data trends are highlighted using heavy broken lines superposed on instantaneous data obtained from DGS. The crack velocity results for the repeatability test can be found in supplementary material Fig. S3. The results generally followed the trends described above except at crack initiation from the initial notch due to loading asymmetries.

4. Stress intensity factor histories

Using the two orthogonal light ray angular deflection fields measured in the global (x, y) coordinates, the instantaneous crack-tip

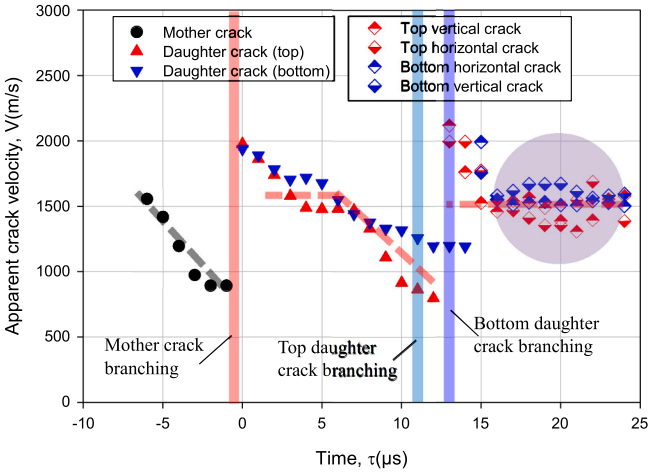

Fig. 10. Apparent/macroscale crack velocity histories from 150 mm × 150 mm soda-lime glass plate. ($\tau = 0$ corresponds to mother crack branching event; the heavy broken lines suggest data trends; data uncertainty during ~3 μs after each branching event is higher than the rest).

fields were computed in the local coordinates (x', y') (with x' coinciding with the instantaneous crack growth direction, making an angle α with respect to the x-axis), for a moving crack via coordinate transformation:

$$\phi_{x'}(t) = \phi_x(t)\, cos\alpha(t) + \phi_y(t)\, sin\alpha(t) \tag{2}$$

The mode-I and mode-II SIFs were then evaluated by analyzing the data around the crack-tip in conjunction with the asymptotic equation (Dondeti and Tippur, 2020);

$$\phi_{x'} = C_\sigma B \left[\begin{array}{c} -\frac{1}{2} r_l^{-\frac{3}{2}} \left\{ f(V; C_L, C_S) A_1(t) cos\left(\frac{3\theta_l}{2}\right) + g(V; C_L, C_S) D_1(t) sin\left(-\frac{3\theta_l}{2}\right) \right\} \\ + \sum_{N=2}^{\infty} \left\{ A_N(t) \left(\frac{N}{2} - 1\right) r_l^{\left(\frac{N}{2}-2\right)} cos\left(\left(\frac{N}{2} - 2\right)\theta_l\right) + D_N(t) \left(\frac{N}{2} - 1\right) r_l^{\left(\frac{N}{2}-2\right)} sin\left(\left(\frac{N}{2} - 2\right)\theta_l\right) \right\} \end{array} \right], \tag{3}$$

using an over-deterministic least-squares error minimization approach. In the above, f and g are functions of instantaneous crack velocity V, and (r_l, θ_l) denote the local crack-tip polar coordinates obtained by contracting the (x', y') in the growth direction as, $r_l = \sqrt{(x')^2 + \alpha_L^2 (y')^2}$ and $\theta_l = tan^{-1}\left(\frac{\alpha_L y'}{x'}\right)$ in the crack growth direction. The coefficients $A_1(t)$ and $D_1(t)$ in the asymptotic series are related to the mode-I and mode-II SIFs, respectively, as $K_I(t) = A_1(t)\sqrt{\frac{\pi}{2}}$ and $K_{II}(t) = D_1(t)\sqrt{\frac{\pi}{2}}$. The functions f and g are given by, $f(V; C_L, C_S) = \left(\frac{1+\nu}{1-\nu}\right) \frac{(1+\alpha_S^2)(1-\alpha_L^2)}{4\alpha_S\alpha_L - (1+\alpha_S^2)^2}$ and $g(V; C_L, C_S) = \left(\frac{1+\nu}{1-\nu}\right) \frac{2\alpha_S(1-\alpha_L^2)}{4\alpha_S\alpha_L - (1+\alpha_S^2)^2}$ where $\alpha_L = \sqrt{1 - \frac{\rho(1-\nu)}{2\mu}V^2}$, $\alpha_S = \sqrt{1 - \frac{\rho}{\mu}V^2}$ for plane stress, μ and ρ are shear modulus and mass density, respectively. For analysis purposes, the data near the crack-tip in the region $0.5 \leqslant r/B \leqslant 1.5$ with an angular extent of $-150° \leqslant \theta_l \leqslant 150°$ was considered. The least-squares analysis was performed with four ($N = 4$) terms in the stress field guided by previous works on this geometry (Dondeti and Tippur, 2020; Sundaram and Tippur, 2018a). In Eq. (3); C_σ is the elasto-optical constant for SLG, and B is the nominal plate thickness.

4.1. 100 mm × 150 mm specimen

The SIF histories extracted from DGS data before crack initiation until branching to post-branching phases of fracture are shown in Fig. 11 (a). Here $\tau = 0$ again corresponds to the mother crack branching event. The mode-I SIF, K_I, (solid black symbols) increased steadily to ~0.75 MPa$\sqrt{m}$ until the crack initiated. Upon crack initiation at the original notch-tip, K_I dropped noticeably for ~2 μs to a value of ~0.6 MPa$\sqrt{m}$ ($=(K_I)_i$) due to unloading. Subsequently, it nearly doubled over the next ~8 μs to ~1.1 MPa$\sqrt{m}$ before branching into two daughter cracks. During the same time period, the mode-II SIF, K_{II}, (open black symbols) values were approx. zero within the accuracy of the SIF extraction scheme used. After branching[6], the magnitudes of K_I decreased (red solid upright triangle for the upper branch, blue solid downward triangle for the lower branch) while K_{II} (red open upright triangle for the upper branch, blue open downward triangle for the lower branch) increased almost instantaneously for each of the mixed-mode daughter cracks. As to be expected, the signs of K_{II} were different for the two daughter cracks in the post-branching regime. The magnitude of both SIFs attained relatively steady values during mixed-mode crack growth over the next 10 μs. The K_{II} values were relatively small when compared to K_I counterparts as the cracks approached a steady growth phase. In Fig. 11(b), the two SIF histories are combined as the effective SIF, $K_{eff}(=\sqrt{K_I^2 + K_{II}^2})$, histories[7]. In the pre- and post-crack initiation phases, K_{eff} trends are approx. same as the ones for K_I in Fig. 11(a). That is, K_{eff} values increase continuously from approx. ~0.6 to ~1.15 MPa$\sqrt{m}$ or the $(K_I)_i$ value approx. doubled during mode-I crack growth phase and then branched at $\tau = 0$. This doubling of K_{eff} could be added into the basket of plausible crack branching precursors along with the crack speed reduction noted earlier. After crack branching and a noticeable drop in K_{eff} values associated with the branching event, a relatively steady value of 0.85 MPa$\sqrt{m}$ is attained by each of the two daughter cracks. These steady values being lower than $2(K_I)_i$ seen when the mother crack branched, no further crack branching from neither of these two daughter cracks occurred in this geometry.

4.2. 150 mm × 150 mm specimen

The histories of the effective SIF, K_{eff}, for the mother crack (solid black circles), the two daughter cracks (red solid upright and blue inverted triangles for the upper and lower branches, respectively) and all four granddaughter cracks (half-filled diamonds, red for the top pair and blue for the bottom pair of granddaughter cracks; the upper and

[6] The SIF data for ~3μs after branching event is more ambiguous relative to pre-branching counterparts.

[7] The effective SIF, $K_{eff}^d = \sqrt{G^d E} = \sqrt{A_1 K_I^2 + A_2 K_{II}^2}$ where G^d is the energy release rate and A_1 and A_2 are functions of instantaneous crack speed [27] . In these experiments, K_{eff}^d was found to be 1.04–1.06 times the corresponding K_{eff}.

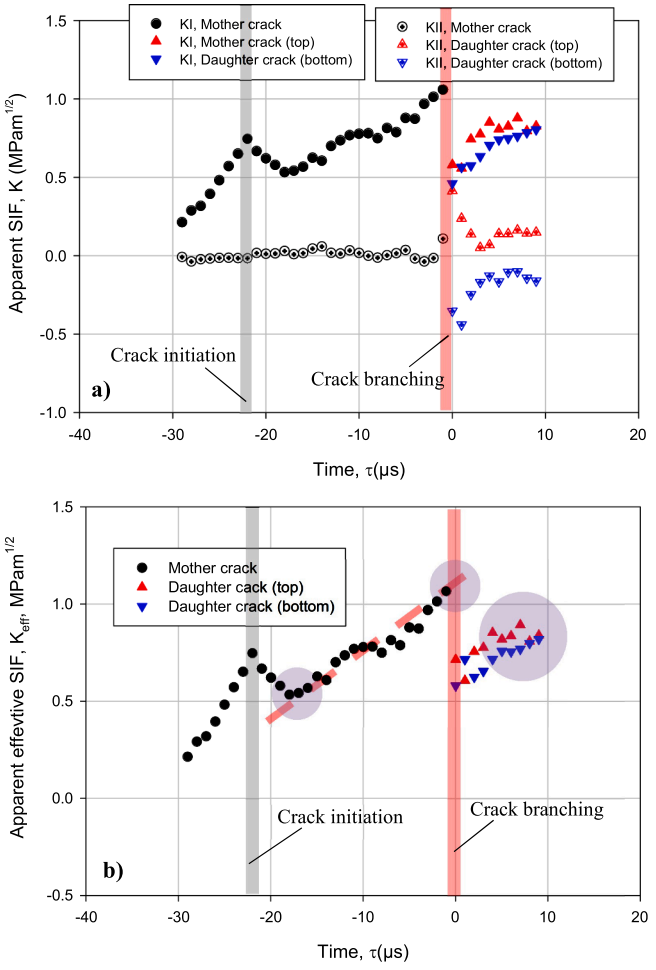

Fig. 11. Stress intensity factor (SIF) histories for 100 mm × 150 mm soda-lime glass plate: (a) Apparent K_I and K_{II}, (b) Effective SIF, $K_{eff} = \sqrt{K_I^2 + K_{II}^2}$. ($\tau$ = 0 corresponds to mother crack branching event; the heavy broken lines suggest data trends; data uncertainty during ~3 μs after each branching event is more than the rest).

lower half-fill correspond to the respective branches) are plotted in Fig. 12 over the window of observation. As in the 100 mm × 150 mm specimen, the increasing trend in K_{eff} to approx. 1.3 MPa$\sqrt{m}$ in the pre-branching phase of the mother crack is evident. Soon after the crack bifurcated, values of K_{eff} each of the two daughter cracks dropped over 2–3 μs period to approx. 0.6 MPa$\sqrt{m}$. This value matches well with the one after crack initiation $(K_I)_i$ in the 100 mm × 150 mm geometry. Subsequently, the values increase to ~1.15 MPa$\sqrt{m}$ for the upper branch and 1.25 MPa$\sqrt{m}$ for the lower branch. These values are approx. twice the post-branching value of ~0.6 MPa$\sqrt{m}$ and also close to the value ($(K_I)_i$) for the mode-I mother crack when it branched at $\tau = 0$ in the smaller size specimen. Again, K_{eff} attaining a value of approx. twice $(K_I)_i$ is similar to the crack branching precursor observed in the 100 mm × 150 mm geometry. The upper branch, however, bifurcated first followed by the lower branch, ~2 μs later. The drop in K_{eff} for each of the resulting four granddaughter cracks is evident but with much more scatter, ranging between 0.5 and 0.9 MPa$\sqrt{m}$, attributed to progressively increasing asymmetries in crack paths resulting in slightly different stress wave emanations and reflections from the newly formed crack faces and free edges of the specimen. Such data scatter and asymmetries are expected to increase further if additional bifurcation events were to occur. However, in this geometry, no further branching of any of the granddaughter cracks occurred. This is consistent with the

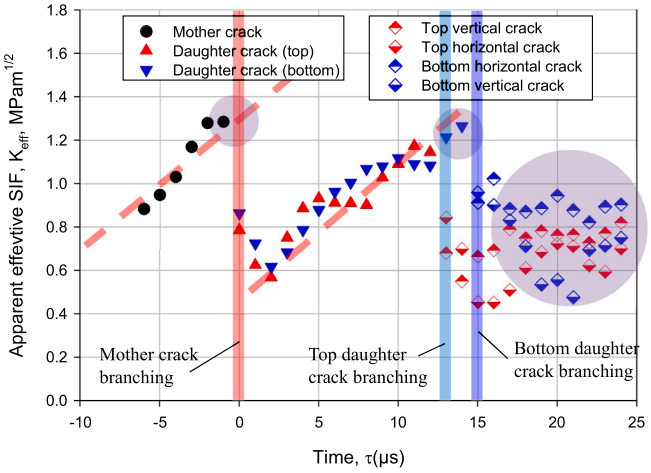

Fig. 12. Effective stress intensity factor ($K_{eff} = \sqrt{K_I^2 + K_{II}^2}$) histories for 150 mm × 150 mm soda-lime glass plate (τ = 0 corresponds to mother crack branching event; the heavy broken lines suggest data trends; data uncertainty during ~3 μs after each branching event is more than the rest).

fact that K_{eff} values for the granddaughter cracks never increased to values above $2(K_I)_i$ seen after crack initiation. (The effective SIF histories for the repeatability test can be found in supplementary material Fig. S4 with data trends same as the one described above.)

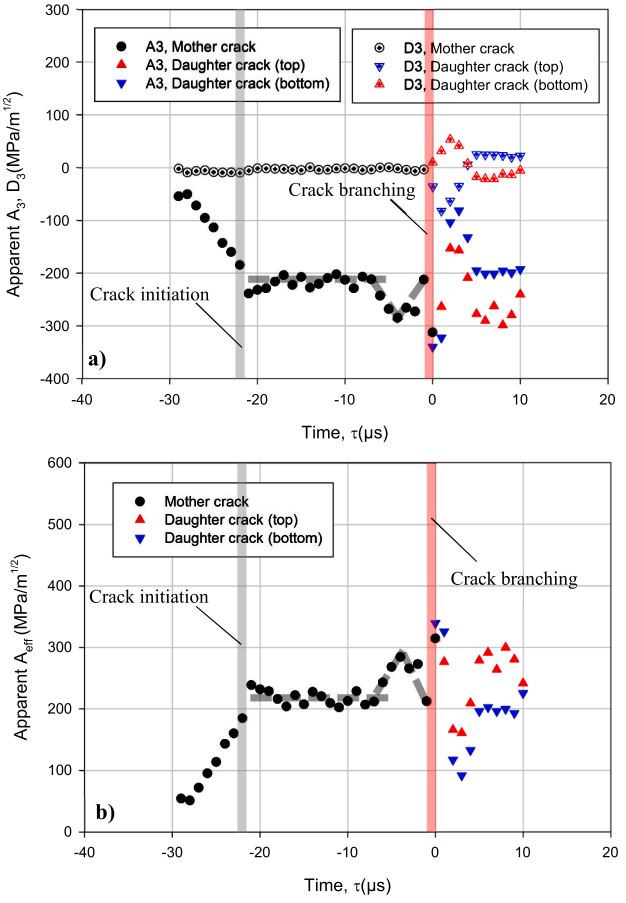

Fig. 13. Higher order term histories for 100 mm × 150 mm soda-lime glass plate: (a) A_3 and D_3, (b) $A_{eff} = \sqrt{A_3^2 + D_3^2}$ (τ = 0 corresponds to mother crack branching event; the heavy broken lines suggest data trends; data uncertainty during ~3 μs after each branching event is more than the rest).

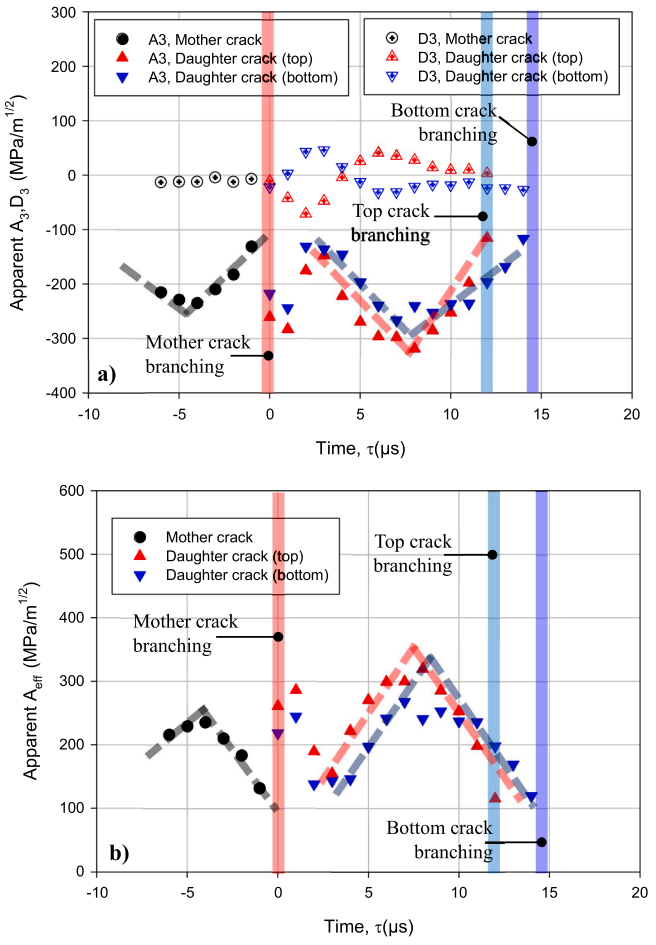

Fig. 14. Higher order term histories for 150 mm × 150 mm soda-lime glass plate: (a) A_3 and D_3, (b) $A_{eff} = \sqrt{A_3^2 + D_3^2}$ ($\tau = 0$ corresponds to mother crack branching event; the heavy broken lines suggest data trends; data uncertainty during ~3 μs after each branching event is more than the rest).

5. Histories of higher order coefficients

In addition to the histories of SIFs, coefficients of higher order terms (HOT) in the asymptotic stress field (see, Eq. (3)) namely, A_3, D_3 were also extracted during the least-squares analysis of stress gradients described earlier. These HOT coefficients are said to account for the specimen geometry and loading configuration under quasi-static conditions and a similar interpretation under dynamic conditions is reasonable. It should be noted that the asymptotic expressions for the fields under consideration are devoid of the coefficients of r^0 term and hence the so-called *T*-stress suggested in the literature (Chao et al., 2001; Ramulu and Kobayashi, 1983; Cotterell and Rice, 1980) to cause (a) curving of crack path during quasi-static growth and (b) branching of crack during dynamic events are not available in DGS measurements. Accordingly, the next dominant coefficients in the field, namely the coefficients of the $r^{1/2}$ term, A_3 and D_3 associated with the symmetric and antisymmetric parts of the asymptotic expansion, respectively, were extracted and examined.

For the 100 mm × 150 mm specimen, histories of A_3, D_3 and $A_{eff}\left(=\sqrt{A_3^2 + D_3^2}\right)$ are plotted in Fig. 13(a) and (b). Being coefficients of the HOT of the asymptotic field, higher degree of noise is to be expected. Before crack initiation, the magnitude of the coefficient of the symmetric part or $|A_3|$ increases monotonically up to initiation (solid back circles) from the notch-tip to approximately 230 MPa/$\sqrt{\text{m}}$ but drops slightly to 210 MPa/$\sqrt{\text{m}}$ following initiation and then remains nearly constant over the next 10 μs of mode-I mother crack growth. At approximately 6 μs prior to the observed crack branching event (at $\tau = 0$), the *magnitude* of A_3 begins to increase to 280–290 MPa/$\sqrt{\text{m}}$ before dropping to ~210 MPa/$\sqrt{\text{m}}$. This results in a noticeable 'V' shaped kink in the data trend, highlighted by the heavy broken gray line superposed on the solid symbols in the plot. During this period leading up to crack branching, the values of the coefficient D_3 (open black symbols) are nearly zero. After the transients associated with crack branch formation[8] have diminished, the mixed-mode daughter cracks attain nearly constant values (solid upright red and downward blue symbols) of −200 and −220 MPa/$\sqrt{\text{m}}$ for the rest of the observation window whereas D_3 values (open upright red and downward blue symbols) attain small negative and positive values, respectively. The A_{eff} trends in Fig. 13(b) are approximately same as the ones for $|A_3|$ in the pre- and post-crack initiation regimes. That is, A_{eff} increased monotonically until crack initiation (solid back circles) to ~200 MPa/$\sqrt{\text{m}}$. Upon crack initiation, A_{eff} values decreased slightly from 240 MPa/$\sqrt{\text{m}}$ to 215 MPa/$\sqrt{\text{m}}$ and continued to be nearly constant for ~10 μs. In pre-branching phase (at τ ~ −6 μs) a noticeable spike or an inverted V-shaped kink is evident in the A_{eff} histories. Interestingly, the increasing trend in the *magnitude* of A_{eff} prior to crack branching event as well as the 'V' shaped kink stands out as a precursor to the impending crack branching event. After the transients associated with the crack branching event diminish, the A_{eff} values don't show any noticeable features that standout and no further macroscale crack branching was observed from neither of the two daughter cracks.

In Fig. 14(a), histories of A_3, D_3 for the 150 mm × 150 mm specimen are plotted. Remembering that the ROI in this geometry was chosen to primarily capture the post-branching behavior, only limited amount of propagation of the mother crack towards its first branching event was monitored at the beginning of the time window. The solid black symbols for the mother crack show the previously noted 'V' shaped kink highlighted by the broken gray trend line prior to the branching event of the mother crack. Once the transients due to branching of the mode-I mother crack diminish, the values of $|A_3|$ for both the daughter cracks show an increasing trend, from 100 to 250 MPa/$\sqrt{\text{m}}$ for the lower branch and 150 to 320 MPa/$\sqrt{\text{m}}$ for the upper branch. Once again, the data for both the mixed-mode daughter cracks show the previously noted 'V' shaped signature in the history (highlighted by the broken red and blue trend lines) before producing a set of two granddaughter crack pairs at 12 and 14 μs. The histories of D_3 for each of these cracks (open blue and red symbols) in the ROI do not show anything distinct *before* the branching event. In Fig. 14(b), A3 and D3 histories are combined as $A_{eff}\left(=\sqrt{A_3^2 + D_3^2}\right)$. As the magnitude of D_3 are small relative to that for A_3, the A_{eff} histories are similar to that of $|A_3|$. That is, A_{eff} histories show a distinct spike or inverted V-shaped kink (again highlighted by the broken red and blue trend lines) before the mother crack branches as well as the two grand-daughter cracks branch. Again, these trends seem consistent not only with that for the mother crack prior to its branching event but also the one observed in the 100 mm × 150 mm geometry. (The A_3, D_3 and A_{eff} histories for the repeatability test can be found in supplementary material Fig. S5. The data trends, however, are noticeably different from the one in Fig. 14 as mother crack initiated in this test as a mixed-mode crack at the notch-tip that eventually followed a dominant mode-I path before branching. Yet, the V-shaped kink features prior to branching are still evident.)

In light of the above observations, one could surmise that the increasing trend in the *magnitude* of A_{eff} as well as the 'V' shaped kink in the data trends for each of the four branching events in the two different geometries standout as potential precursors of the bifurcation event.

[8] The HOT data for ~3μs after each branching event is relatively more ambiguous when compared to pre-branching counterparts.

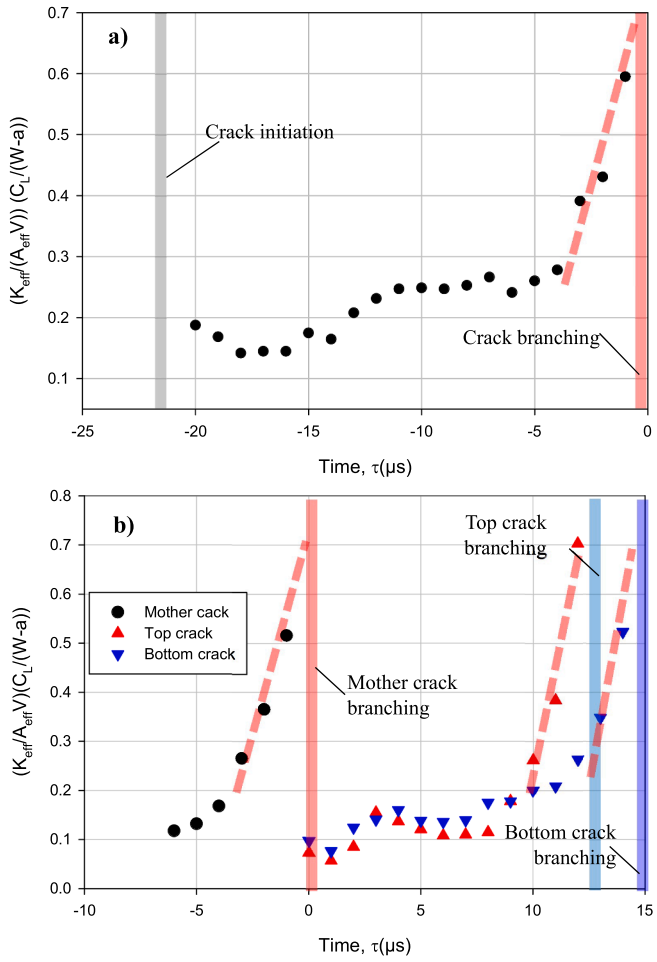

Fig. 15. Non-dimensional parameter, $\widehat{K} = \left(\frac{K_{eff}}{A_{eff}V}\right)\left(\frac{C_L}{W-a}\right)$ histories from DGS for a) 100 mm × 150 mm and b) 150 mm × 150 mm soda-lime glass plates. (τ = 0 corresponds to mother crack branching event; the heavy broken lines highlight approx. data trends.)

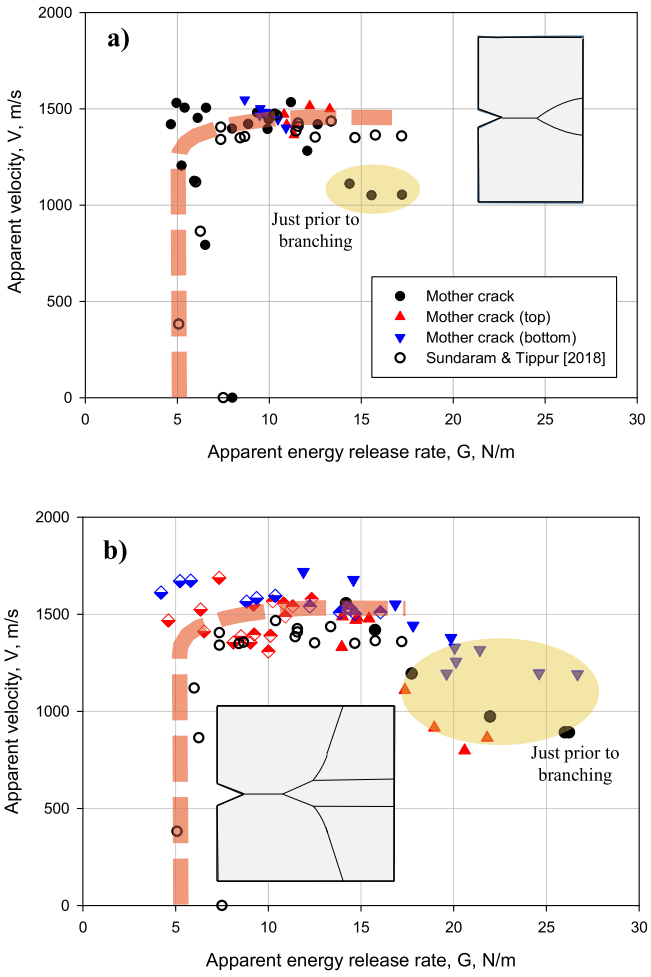

Fig. 16. Variation of apparent energy release rate (G) with apparent crack velocity (V) from DGS for a) 100 mm × 150 mm and b) 150 mm × 150 mm soda-lime glass plates. (The heavy broken lines and shaded zones are manually overlaid to suggest data trends.)

6. Discussion

The crack growth results presented above from two different SLG specimen geometries subjected to nominally identical loading present several unique features prior to crack bifurcation. The optically measured fracture parameters and resulting data trends leading up to the single and triple crack bifurcations seen in these two geometries, apparent (or macroscale) crack speed V, apparent effective SIF K_{eff}, and higher order coefficent A_{eff}, all exhibit distinct signatures/features. The apparent crack velocity (V) prior to crack branch formation in each of the instances dropped from a relatively steady value of ~1500 m/s to ~1000 m/s. This feature was seen consistently in each of the four crack bifurcation events in the two mode-I and two mixed-mode cracks, and hence qualifies to be considered a macroscale precursor of bifurcation event. A monotonic increase of the effective SIF (K_{eff}) and more importantly the doubling of its value, from $(K_I)_i$of ~0.6 MPa$\sqrt{m}$ to ~1.2 MPa$\sqrt{m}$ for SLG, was also observed consistently prior to each of the crack bifurcation events and is a second precursor of branching. Lastly, the higher order coefficient A_{eff} extracted prior to each of the branching events consistently showed roughly an 'inverted V' shaped kink in the data trend for all four bifurcation events. The change in the slope of A_{eff} prior to each of the branching events stands out as another precursor.

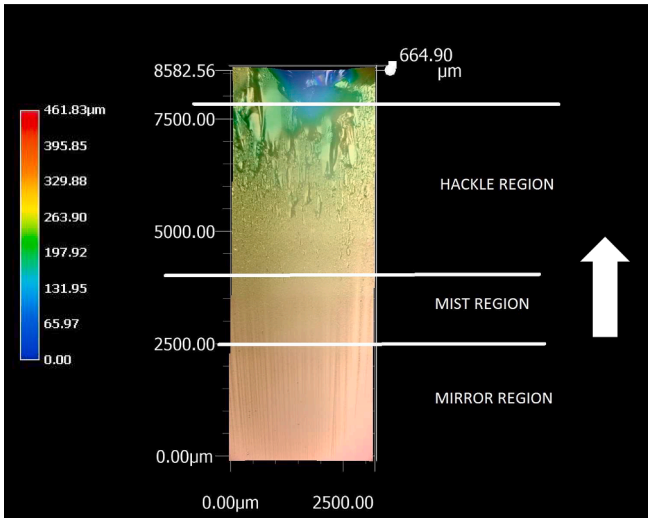

Fig. 17. Digitally stitched image of fractured surface for 100 mm × 150 mm and soda-lime glass plates. (The arrow indicates crack growth direction.)

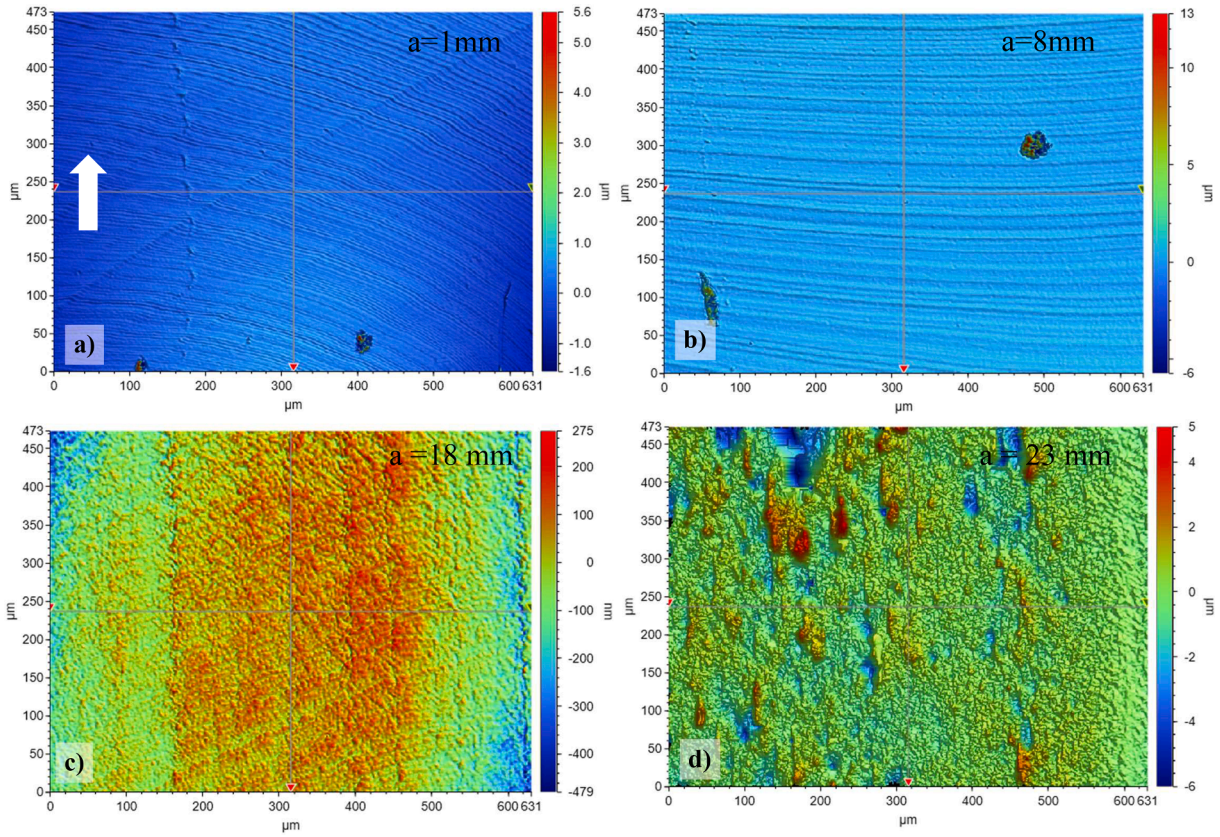

Fig. 18. Images of the fractured surface at different distances from the initial notch front obtained from optical profilometer for 100 mm × 150 mm. (The white arrow indicates crack growth direction.)

Based on the above three different crack branching precursors identified via direct optical measurements, a combined non-dimensional crack bifurcation parameter, $\widehat{K} = \left[\left(\frac{K_{eff}}{A_{eff}(W-a)}\right)\left(\frac{C_L}{V}\right)\right]$ was also formulated. Here, C_L is the longitudinal wave speed in SLG, a is instantaneous crack length, W is the width of the specimen in the crack growth direction and $A_{eff} = \sqrt{A_3^2 + D_3^2}$. The histories of $\widehat{K}$ are plotted in Fig. 15 for both the specimen geometries (and Fig. S6 in the supplementary material). Based on the data trends, a sharp rise in the *magnitude* of $\widehat{K}$ prior to branching event is consistently evident and also serves as a LEFM-based precursor of crack bifurcation. A 3–4 fold increase in the magnitude of $\widehat{K}$ at branching is notable in each of these plots. The universality of the parameter, however, needs to be further tested by investigating similar behaviors in other amorphous brittle materials to fully understand its physical meaning. Furthermore, it should also be noted that these precursors are limited to the impending crack bifurcation but they do not indicate the direction of the daughter and granddaughter cracks. Therefore, additional work, possibly by considering the so-called *T*-stress (or, σ_{0x} in the experimental mechanics community) in addition to the precursors identified in this work, is necessary as well.

The relationship between instantaneous energy release rate G^d and crack velocity V in both these geometries were also assessed by computing the former using $G^d E = A_1 K_I^2 + A_2 K_{II}^2$ for plane stress conditions where E is the elastic modulus of SLG and A_1, A_2 are velocity dependent functions (Ravi-Chandar, 2004). The results are shown in Fig. 16(a) and (b) for the two specimen geometries and Fig. S7 of the supplementary material[9]. The data from Sundaram and Tippur's (Sundaram and Tippur, 2018a) work (open symbols) are also superimposed on the current ones. Given the potential experimental errors involved in both the measured quantities of these graphs, the agreement is rather good. The overall trendline of the data is also suggested and the cluster of data points corresponding to just prior to branching seem to be outliers to the overall *G-V* trend.

Linking the macroscale optical measurements with microscale fracture surface features could be a way forward for understanding crack branching better. Accordingly, an attempt to link LEFM-based parameters to the fracture surface features extracted via post-mortem fractography was carried out. First, a Keyence digital microscope (VHX-6000, resolution 1 μm) was used to examine the surface features by photographing the fractured surfaces in different regions, starting from the initial notch front zone to where the crack branched macroscopically. A digitally stitched, pseudo-colored image of the same for the 100 mm × 150 mm sample is shown in Fig. 17[10]. As reported in several previous dynamic crack growth investigations on in amorphous brittle polymers and glasses, the 'mirror-mist-hackle' zones are evident in this image (Ravi-Chandar and Knauss, 1984; Sundaram and Tippur, 2018a). Similar features were also observed in 150 mm × 150 mm sample prior to and after each of the three branching events and are not shown here for brevity. The accuracy of the digital microscope, however, was found insufficient to capture detailed surface features and quantify the roughness in the mirror region and early stages of the mist region. Hence, an optical profilometer (Bruker Contour Elite K 3D, resolution 10 nm) was used for further analysis of the 100 mm × 150 mm specimen surface. Fractography of discrete locations along the centerline of the fracture surface over approximately 0.63 × 0.47 mm region in 1 mm

[9] The data corresponding to the first 3μs *after* each branching event are excluded due to higher degree of uncertainty.

[10] The region very close to the initial notch front is excluded from the image; the arrow mark indicates the crack growth direction.

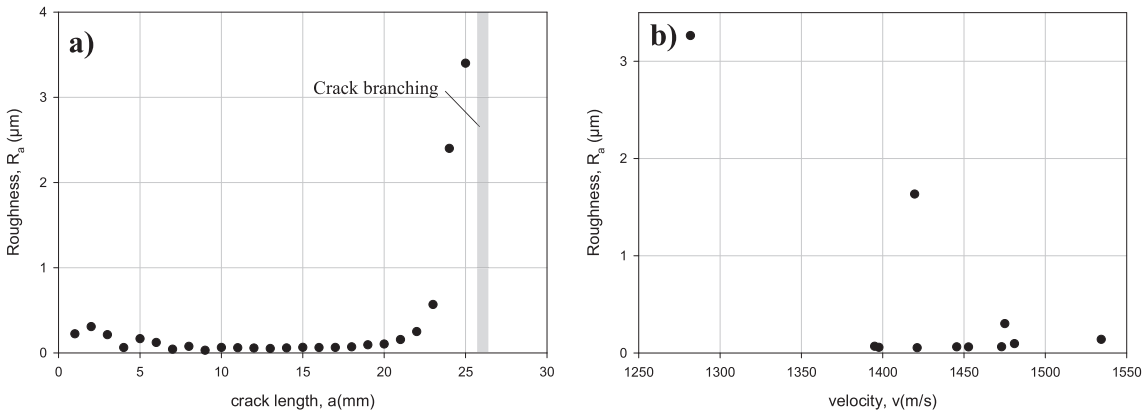

Fig. 19. (a) Variation of surface roughness (R_a) at different distances from the initial crack front and (b) Variation of (R_a) with crack velocity for 100 mm × 150 mm specimen. (The lack of any correlation between surface roughness and crack speed is noticeable.)

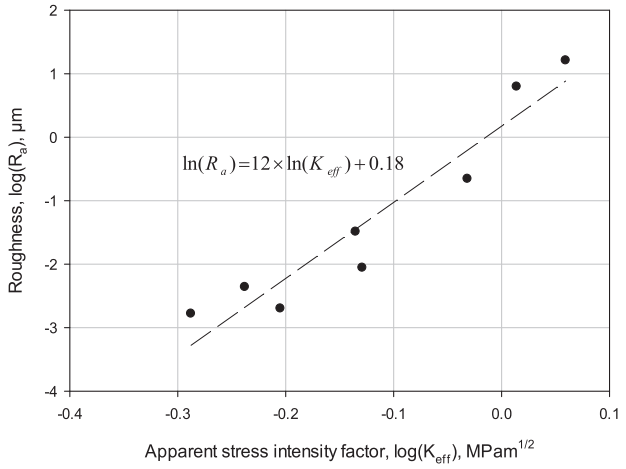

Fig. 20. Variation (linear fit) of surface roughness, log(R_a) with apparent effective stress intensity factor, K_{eff} for 100 mm × 150 mm soda-lime glass plate.

steps, from the initial notch front to where the crack branched (or, the hackle region), was undertaken. A few select pseudo-colored images of those measurements are shown in Fig. 18 corresponding to the mirror, mist, and hackle zones. (Note that the surface profile scales are different in each of these images due to vast differences in scales.) In the mirror and mist regions (Fig. 18(a), (b)), periodic and curved striations representing the so-called Wallner lines, caused by the interference of stress waves emanating from the growing crack with those reflected off the free specimen surfaces, are evident. Apart from this, the surface is relatively featureless when compared to quasi-brittle polymers (Ravi-Chandar and Knauss, 1984) which commonly show conic marks attributed to material inhomogeneities and defects. The Wallner lines become less discernable when the crack enters the mist and hackle zones (Fig. 18 (c), (d)) where there is significantly higher surface roughness relative to the mirror region. A plot of the surface roughness (averaged over 0.63 mm × 0.47 mm) along the crack path where the crack branches in the specimen is plotted in Fig. 19(a). A roughness value of R_a ~0.25 μm soon after crack initiation from the notch drops to 30–80 nm range until the crack grows by approx. 20 mm. Next, a steep rise in R_a to 3–4 μm is evident as the crack enters the 'hackle' phase. The trend line for R_a extrapolates to ~6 μm at crack branching. It is worth noting that Sundaram and Tippur, 2018a, who used a coarser contact-type surface profiler, also noted a similar value of roughness in the hackle region prior to branching. Fig. 19(b) shows variation of R_a as a function of crack velocity. Note that the number of data points is different in this plot relative to Fig. 19(a) since velocity data was obtained from optical measurements and not from fractography. Evidently, there is no obvious correlation between the two measurements in Fig. 19(b). This is unlike a few other investigations on dynamic fracture of quasi-brittle polymers (Arakawa and Takahashi, 1991; Hull, 1996; Takahashi et al., 1998). The measured roughness obtained from fractography was examined relative to the corresponding (effective) stress intensity factors in Fig. 20. Note that log(R_a) is plotted with K_{eff} in light of the power-law type variation evident in Fig. 20. An approximately linear variation of log(R_a) with K_{eff} is evident.

7. Conclusions

Full-field quantitative visualization of time-resolved stress gradients near dynamically growing cracks in soda-lime glass plates of two different geometries subjected to nominally identical symmetric stress wave loading was undertaken using the Digital Gradient Sensing (DGS) technique. The first geometry produced a single crack bifurcation event; a dynamically propagating mode-I mother crack branched into two globally symmetric mixed-mode daughter cracks. The second geometry produced three cascading crack bifurcation events; a dynamically growing mode-I mother crack bifurcated into two globally symmetric mixed-mode daughter cracks, each of which bifurcated again into two granddaughter cracks subsequently. The optical measurements were utilized to quantify fracture parameter histories during various fracture events. Subsequently, LEFM-based precursors prior to each of the bifurcation events were identified. They included crack velocities (V), effective stress intensity factors (K_{eff}), higher order coefficients (A_{eff}) of the asymptotic crack-tip fields. A non-dimensional parameter based on these three measured quantities, $\widehat{K}$, was also formulated. Furthermore, relationships between instantaneous energy release rate, G and crack velocity, V were obtained. Fracture surface roughness and other fractographic features were also separately quantified via high resolution post-mortem study and examined relative to the optical measurements. The main results of this work can be summarized as follows:

- A drop in the macroscale (apparent) crack velocity V from a steady value of ~1500 m/s to ~1000 m/s was observed consistently when crack branching was imminent in both single and cascading branch formation geometries.
- The cracks bifurcated when K_{eff} reached approximately twice the value at initiation (~0.6 MPa$\sqrt{\text{m}}$) in both the single and cascading branch formation geometries.
- The cracks bifurcated after the higher order coefficient of the asymptotic field A_{eff} showed a distinct kink in the data trend.
- Energy release rates showed strong dependence with crack speeds in all experiments. Due to the drop in the crack speed prior to each

bifurcation event, the *G-V* trends contain a cluster of data points just before crack bifurcation.

- A non-dimensional parameter $\widehat{K}$, formulated using measured V, K_{eff}, and A_{eff}, consistently showed a steep raise prior to each crack bifurcation.
- The surface roughness showed the mirror-mist-hackle features but without conic marks seen in quasi-brittle polymers.
- The fracture surface roughness (R_a) was quantified in each of mirror-mist-hackle zones and a power-law type variation was observed with K_{eff} and $\widehat{\sigma}$. A linear relationship between $\log(R_a)$ and K_{eff} was obtained.
- The crack bifurcation angles based on measured parameters is, however, lacking in this investigation. Evaluation of the *T*-stress from measurements is a possible way to address this shortcoming via additional experiments and numerical simulation of the reported experiments.

Declaration of Competing Interest

The authors declare that they have no known competing financial interests or personal relationships that could have appeared to influence the work reported in this paper.

Acknowledgements

Partial support for this research through Army Research Office grants W911NF-16-1-0093, W911NF-15-1-0357 (DURIP) and W911NF-17-1-0355-RI are gratefully acknowledged. Authors also acknowledge the assistance of Drs. Kyle Schulze and Nima Shamsaei during microscopy and fractography.

Appendix A. Supplementary data

Supplementary data to this article can be found online at https://doi.org/10.1016/j.ijsolstr.2021.111252.

References

Arakawa, K., Takahashi, K., 1991. Relationships between fracture parameters and fracture surface roughness of brittle polymers. Int. J. Fract. 48 (2), 103–114.
Bieniawski, Z.T., 1968. Fracture dynamics of rock. Int. J. Fract.Mech. 4 (4), 415–430.
Bobaru, F., Zhang, G., 2015. Why do cracks branch? a peridynamic investigation of dynamic brittle fracture. Int. J. Fract. 196 (1-2), 59–98.
Chao, Y.J., Liu, S., Broviak, B.J., 2001. Brittle fracture: variation of fracture toughness with constraint and crack curving under mode I conditions. Exp. Mech. 41 (3), 232–241.
Cotterell, B., Rice, J.R., 1980. Slightly curved or kinked cracks. Int. J. Fract. 16 (2), 155–169.
Dally, J.W., 1979. Dynamic photoelastic studies of fracture. Exp. Mech. 19 (10), 349–361.
Döll, W., 1975. Investigations of the crack branching energy. Int. J. Fract. 11 (1), 184–186.
Dondeti, S., Tippur, H.V., 2020. A comparative study of dynamic fracture of soda-lime glass using photoelasticity, digital image correlation and digital gradient sensing techniques. Exp. Mech. 60 (2), 217–233.
Eshelby, J.D., 1999. Energy relations and the energy-momentum tensor in continuum mechanics. In: Ball, J.M., Kinderlehrer, D., Podio-Guidugli, P., Slemrod, M. (Eds.), Fundamental Contributions to the Continuum Theory of Evolving Phase Interfaces in Solids. Springer Berlin Heidelberg, Berlin, Heidelberg, pp. 82–119.
Ha, Y.D., Bobaru, F., 2010. Studies of dynamic crack propagation and crack branching with peridynamics. Int. J. Fract. 162 (1-2), 229–244.
Hawong, J.S., Kobayashi, A.S., Dadkhah, M.S., Kang, B.-S.-J., Ramulu, M., 1987. Dynamic crack curving and branching under biaxial loading. Exp. Mech. 27 (2), 146–153.
Hull, D., 1996. Influence of stress intensity and crack speed on fracture surface topography: mirror to mist to macroscopic bifurcation. J. Mater. Sci. 31 (17), 4483–4492.
Karma, A., Lobkovsky, A.E., 2004. Unsteady crack motion and branching in a phase-field model of brittle fracture. Phys. Rev. Lett. 92 (24), 245510.
Mehrmashhadi, J., Bahadori, M., Bobaru, F., 2020. Comparison of peridynamic and phase-field models for dynamic brittle fracture in glassy materials. engrXiv 1–29S.
Miao, C., Tippur, H.V., 2020. Dynamic fracture of soda-lime glass plates studied using two modified digital gradient sensing techniques. Eng. Fract. Mech. 232, 107048.
Periasamy, C., Tippur, H.V., 2013. Measurement of orthogonal stress gradients due to impact load on a transparent sheet using digital gradient sensing method. Exp. Mech. 53 (1), 97–111.
Prautzsch, H., Boehm, W., Paluszny, M., 2013. Bézier and B-spline techniques. Springer Science & Business Media.
Kobayashi, A., Kang, B.-J., 1984. Dynamic crack branching—a photoelastic evaluation. In: Fracture Mechanics: Fifteenth Symposium. ASTM International.
Ramulu, M., Kobayashi, A.S., 1983. Dynamic crack curving—a photoelastic evaluation. Exp. Mech. 23 (1), 1–9.
Ravi-Chandar, K., Knauss, W.G., 1984. An experimental investigation into dynamic fracture: III. On steady-state crack propagation and crack branching. Int. J. Fract. 26 (2), 141–154.
Ravi-Chandar, K., Knauss, W.G., 1984. An experimental investigation into dynamic fracture: II. Microstructural aspects. Int. J. Fract. 26 (1), 65–80.
Ravi-Chandar, K., Dynamic Fracture. 2004: Elsevier.
Rose, L., 1976. Recent theoretical and experimental results on fast brittle fracture. Int. J. Fract. 12 (6), 799–813.
Schardin, H., 1959. Velocity effects in fracture. Fracture (Edited by Averbach et al.). John Wiley.
Sundaram, B.M., Tippur, H.V., 2016. Dynamics of crack penetration vs. branching at a weak interface: an experimental study. J. Mech. Phys. Solids 96, 312–332.
Sundaram, B.M., Tippur, H.V., 2018(a). Dynamic fracture of soda-lime glass: a full-field optical investigation of crack initiation, propagation and branching. J. Mech. Phys. Solids 120, 132–153.
Sundaram, B.M., Tippur, H.V., 2018(b). Full-field measurement of contact-point and crack-tip deformations in soda-lime glass. Part-I: Quasi-static Loading. Int. J. Appl. Glass Sci. 9 (1), 114–122.
Sundaram, B.M., Tippur, H.V., 2018(c). Full-field measurement of contact-point and crack-tip deformations in soda-lime glass. Part-II: Stress wave loading. Int. J. Appl. Glass Sci. 9 (1), 123–136.
Takahashi, K., Kido, M., Arakawa, K., 1998. Fracture roughness evolution during mode I dynamic crack propagation in brittle materials. Int. J. Fract. 90 (1–2), 119–131.
Theocaris, P.S., Andrianopoulos, N.P., Kourkoulis, S.K., 1989. Crack branching: a "twin-crack" model based on macroscopic energy fracture criteria. Eng. Fract. Mech. 34 (5-6), 1097–1107.
Xu, X.-P., Needleman, A., 1994. Numerical simulations of fast crack growth in brittle solids. J. Mech. Phys. Solids 42 (9), 1397–1434.
Yoffe, E.H., LXXV, 1951. The moving griffith crack. The London, Edinburgh, and Dublin Philosophical Magazine and Journal of Science 42 (330), 739–750. https://doi.org/10.1080/14786445108561302.
Zeng, Q., Motamedi, M.H., Leong, A.F.T., Daphalapurkar, N.P., Hufnagel, T.C., Ramesh, K.T., 2019. Validated simulations of dynamic crack propagation in single crystals using EFEM and XFEM. Int. J. Fract. 215 (1-2), 49–65.
Zhou, F., Molinari, J.F., 2004. Dynamic crack propagation with cohesive elements: a methodology to address mesh dependency. Int. J. Numer. Meth. Eng. 59 (1), 1–24.